ADVANCED FUNCTIONAL MATERIALS
www.afm-journal.de

2D Ruddlesden-Popper Perovskites/PVDF-TrFE Photodetector for Anti-Interference Vision System Derived from Ferroelectric Polarization Modulation

*Xinglong Zhang, Enliu Hong, Xiaojun Tan, Jie Liu, Anquan Jiang, and Xiaosheng Fang**

2D Ruddlesden-Popper (RP) perovskites have garnered increasing attention for their excellent photoresponse, characterized by high carrier mobility, tunable bandgaps, high optical absorption, and molecular asymmetry. Herein, centimeter scale single crystal 2D hybrid perovskites, BA_2PbBr_4 (BPB) is synthesized, using quasi-static cooling method and composited with ferroelectric PVDF-TrFE(PT) film to construct a multi-field coupling photodetector (PD) via van der Waals force contact. Ferroelectric tests show that the PT film exhibits a saturated polarization strength of 3.6 μC cm^{-2}, allowing the ferroelectric localized field to modulate the band structure of PT and enhance the photocurrent. The Heterojunction systems exhibit ultra-high responsivity (15.3 A W^{-1}) and detectivity (1.99 × 10^{13} Jones) under 390 nm illumination at 3 V bias, with a performance improvement of over 10^2 times compared to BPB PDs. Furthermore, the hybrid PDs exhibit highly stable *I–t* curve with a photocurrent retention rate of 97.4%. Leveraging this feature, a large-area imaging device is designed at the centimeter level scale, enabling multifunctional vision applications accurate letter imaging process and anti-interference number detection. The work presents a valuable insight in design of future autonomous driving vision systems.

1. Introduction

In recent years, 2D organic-inorganic hybrid perovskites have shown great potential in optoelectronics and smart devices due to their large carrier mobility, tunable bandgaps, high optical absorption, molecular asymmetry, etc.[1–7] 2D Ruddlesden-Popper (RP) perovskites can be described by the general formula $(RNH_3)_2A_nX_{3n+1}$, where R is an alkyl or aromatic group, A is a metal cation and X is a halide anion.[8–10] Compared to 3D perovskites, 2D RP perovskites display enhanced photoresponse due to their large organic cations, which increase excitation binding energy and lower defect state density.[11–15] Besides, the large organic cations in 2D RP perovskites endow themselves with higher hydrophobicity to keep the layered perovskites from moisture and oxygen infiltration, contributing to their long-term environmental stability.[16–20]

To date, numerous 2D hybrid perovskites with excellent photoresponse and ferroelectricity have been reported. It is worth noting that a quasi-static cooling method (≈1 K day^{-1}) has been employed to prepare a series of centimeter-scale 2D perovskites, including $BA_2MA_2Pb_3Br_{10}$,[21] $IBA_2EA_2Pb_3I_{10}$,[22] $PZPbCl_3$,[23] (4ABA)PbI_4,[24] etc. Specifically, researchers successfully synthesized $(IBA)_2MHy_2Pb_3Br_{10}$ perovskites which exhibited bulk photovoltage via introducing the stereo-chemically active lone pair perovskitizer.[25] In addition, the perovskites exhibited ultra-highly sensitive polarized photodetection (polarization ratio up to 24.6), outstanding responsivity (200 mA W^{-1}) and detectivity (2.4 × 10^{13} Jones). Furthermore, a novel 2D hybrid perovskite photodetector(PD) ($BBA_2EA_2Pb_3Br_{10}$) with a high Curie temperature (425K) and notable pyroelectric coefficient (5.4 × 10^{-3} μC cm^{-2} K^{-1}) was successfully synthesized.[26] More importantly, this PD exhibited high responsivity (0.28 mA W^{-1}) and specific detectivity (1.31 × 10^{10} Jones) at 0 V bias. In addition, a universal low-temperature vapor-phase synthesis method[27] of ultrathin perovskites with size up to 1.5 ×1.5 cm^2 was developed. The perovskites in this study displayed excellent optoelectronic performance with superior responsivity (3.7 × 10^3 A W^{-1}) and ultrafast response time (≈10 μs).

At present, ferroelectric materials have shown broad applications in energy storage,[28] optoelectronics,[29–31] field-effect transistors,[32,33] information storage,[34,35] memristors,[36] etc. The permanent electrical polarization in the ferroelectric materials enables the effective tuning of internal carrier concentration in PDs, which enhances the photoresponse

X. Zhang, E. Hong, J. Liu, X. Fang
Department of Materials Science
State Key Laboratory of Molecular Engineering of Polymers
Fudan University
Shanghai 200433, P. R. China
E-mail: xshfang@fudan.edu.cn
X. Tan
Shaoxin Laboratory
Shaoxing 312000, P. R. China
A. Jiang
State Key Laboratory of ASIC&System
School of Microelectronics
Fudan University
Shanghai 200433, P. R. China
The ORCID identification number(s) for the author(s) of this article can be found under https://doi.org/10.1002/adfm.202424848

DOI: 10.1002/adfm.202424848

of PDs through energy band regulation.[37] In recent years, poly(vinylidene fluoride-trifluoroethylene)ferroelectric films has been used in nano and smart electronic devices.[38–40] PVDF is based on the —CH_2—CF_2—vinylidene (VDF) monomer and categorized to four polymorphs (α, β, δ, and γ) according to the different molecular chain conformations.[41] The β phase, with its unit cell consisting of two all-trans conformation chains, exhibits high polarization. However, pure PVDF is non-polar and paraelectric under ambient conditions, which requires further processing to generate ferroelectricity. To address this, the second monomer molecules such as trifluoroethylene (TrFE) and tetrafluoroetgylene (TFE) are often introduced into the PVDF, to obtain a copolymer with better stability and superior ferroelectric properties under ambient conditions.[42–44] Researchers designed a PD based on MoS_2 transistor with PVDF-TrFE(PT) ferroelectric gate.[45] The PT is employed to depress the dark current of MoS_2 semiconducting channel. The stable remnant polarization in PVDF-TrFE can provide an ultrahigh local electrostatic field (10^9 V m^{-1} within nanometer scale) The photodetector exhibited high responsivity (2570 A W^{-1}) and detectivity (2.2×10^{12} Jones).

Inspired by the previous work, we synthesized centimeter-scale 2D RP perovskites BA_2PbBr_4 (BPB) using quasi-static cooling method. Subsequently, we prepared PT films using a spin coating method. Then, we constructed a heterojunction photodetection system via van der Waals contact between BPB and PT film, which exhibited ultrahigh responsivity (15.3 A W^{-1}), detectivity (1.99×10^{13} Jones), and high stability under 390 nm illumination at 3 V bias. Notably, the responsivity and detectivity were improved over 10^2 times than that of BPB PDs. Leveraging this feature, we developed a multifunctional, centimeter-scale imaging device. The BPB/PT imaging system generated higher photocurrent compared to the imaging system of BPB alone, resulting in higher contrast and superior image quality. Moreover, the BPB/PT imaging demonstrated excellent detection accuracy in anti-interference vision system, both before and after interference. Our work provides a novel approach for integrating 2D RP perovskites into future autonomous vehicle vision detection.

2. Results and Discussion

As illustrated in **Figure 1a**, centimeter-scale BPB perovskites single crystals are obtained through a quasi-static cooling crystallization process. Subsequently, PT ferroelectric films were prepared using spin coating method. By adjusting the rotational speed, a series of PT films with different thicknesses were synthesized. The PD was then constructed by combining BPB perovskites with PT ferroelectric film via Van der Waals contact. Finally, a 6×6 array light imaging device was obtained after thermal evaporation of gold electrodes. Figure 1b shows the typical crystal structure of BPB, which belongs to typical 2D RP perovskites. According to previous study,[9] the nucleation energy barrier is defined as the difference between the free energy of molecules in nucleated particles and their energy in solution:

$$\Delta G_{solution} = 4\pi r^2\gamma + \frac{4}{3}\pi r^3\left(-\varepsilon + \varepsilon_A - k_B T \ln N_A\right) = \frac{16\pi}{3} \times \frac{\gamma^3}{\left(\varepsilon - \varepsilon_A + k_B T \ln N_A\right)^2} \quad (1)$$

where r is the critical nucleus radius, γ is the crystallite's surface energy, ε is the cohesive energy of precursor molecules in the cluster, ε_A is the molecular binding energy, k_B is the Boltzmann constant, T is the temperature and N_A is the mole fraction of isolated molecules. In comparison to the solution volume, the precursor molecule in the surface layer experience tension-related elastic energy, denoted as ε_A-$\varepsilon_{surface}$. The nucleation energy barrier at the solution surface is:

$$\Delta G_{surface} = \frac{16\pi}{3} \times \frac{\gamma^3}{\left(\varepsilon - \varepsilon_A + \varepsilon_{surface} + k_B T \ln N_A\right)^2} \quad (2)$$

Comparing Equations (1) and (2), the nucleation energy barrier at the solution surface is lower than that in the solution volume (Figure 1c), indicating that nucleation occurs more easily at the surface. According to the transition state theory, at the gas-liquid interface, precursor molecules possess higher chemical potential in their initial state due to the surface energy effect (Figure S3, Supporting Information). Consequently, the crystal growth preferentially occurs along along the plane parallel to the solution surface, with the growth rate along this direction being faster than in the vertical direction. Buoyancy and surface tension cause the crystals to float on the surface of the solution, growing at different rates along different crystal planes (Figure S4, Supporting Information).

As shown in Figure 1d, the BPB single-crystal microsheet exhibits a regular rectangular morphology with dimensions of 30 × 20 µm. Figure 1e demonstrates that the BPB single-crystal microsheet has a thickness of 23 nm. The laser confocal 3D height image of BPB perovskites is presented in Figure S5 (Supporting Information). From the scanning electron microscope (SEM) image in Figure S6 (Supporting Information), the BPB single crystals clearly show their regular rectangular morphology. Figure S7 (Supporting Information) presents the transmission electron microscope (TEM) image of BPB perovskite nanosheets obtained by ultrasonic dispersion. As displayed in Figure 1f, the high-resolution TEM image of BPB nanoplates exhibits clear lattice fringes and excellent interplanar atomic arrangement, indicating high crystallinity and quality. The interplanar spacing is measured at 0.21 nm, corresponding to the (002) facet of BPB perovskites the inset shows the corresponding fast Fourier transform (FFT) pattern of BPB. Figure S8 (Supporting Information) illustrates the schematic diagram for calculating the BPB crystal plane spacing. Furthermore, the sharp diffraction spots observed in the corresponding selected area electron diffraction (SAED) pattern in Figure 1g confirm the single-crystalline nature of the BPB nanoplate, with spots corresponding to (002) and (004) facets.

As displayed in Figure S9a (Supporting Information), the XRD results demonstrate that BPB is a single-crystal material with sharp and high-intensity peaks. The diffraction peaks at 2θ = 6.3°, 12.7°, 19.1°, 25.7°, 32.3°, and 39.0° correspond to (002), (004), (006), (008), (0010) and (0012) facets of BPB, consistent with stimulation results. According to the XPS survey spectrum (Figure S9b, Supporting Information), the BPB perovskites are composed of C, N, Pb, and Br with an O peak attributed to surface oxidation. In the high-resolution C 1s XPS spectrum (Figure S9c, Supporting Information), three peaks at 283.4, 284.6, and 285.2 eV are observed, corresponding to C—H

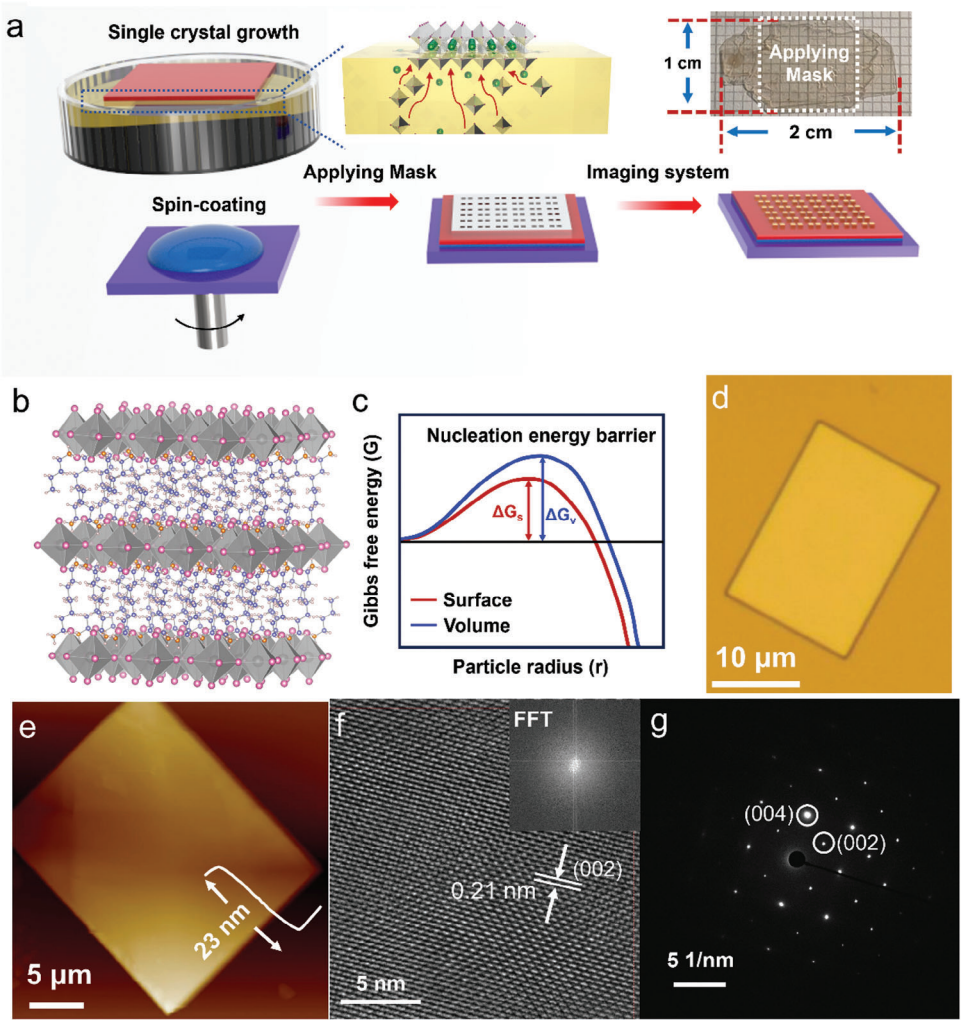

Figure 1. Growth and structure characterization of 2D BPB perovskites. a) Schematic diagram of fabrication process of large area BPB/PT light imaging system. b) Crystal structure of BPB perovskites. c) Comparison of nucleation barriers between the solution surface and volume. d) Optical morphology of BPB perovskites. e) corresponding AFM image of BPB perovskites. f) High-resolution TEM image of BPB perovskites. The inset shows the corresponding FFT image. g) SAED patterns of BPB perovskites.

bond, standard C 1s, and C—C bond, respectively. The high-resolution N 1s XPS spectrum (Figure S9d, Supporting Information) shows peaks at 400.9 eV. In Figure S9e (Supporting Information), the Pb 4f peaks are located at 137.2 and 142.5 eV, corresponding to the characteristic doublet state Pb $4f_{7/2}$ and Pb $4f_{5/2}$. The high-resolution Br 3d XPS spectrum shows peaks at 67.4 and 68.6 eV, corresponding to the characteristic doublet state Br $3d_{5/2}$ and Br $3d_{3/2}$ (Figure S9f, Supporting Information). According to the UV–vis absorption spectrum (Figure S9g, Supporting Information), BPB perovskites exhibit a sharp absorption edge at 425 nm, with an optical bandgap estimated to be 2.83 eV, as determined by the Tauc plot (Figure S9h, Supporting Information). As displayed in Figure S9I (Supporting Information), the wavelength peak of room-temperature PL emission spectrum is located at 412 nm. Figure S10 (Supporting Information) shows the optical image of a series of centimeter-sized single-crystalline BPB perovsites obtained from the quasi-static cooling method.

As shown in **Figure 2a**, in the device for conducting ferroelectric domain switching performance tests of PT, the bottom electrode is ITO glass and the top electrode is gold and the electrode area is 2 × 2 mm^2. Herein, we adopt crossed areas for the performance test between top and bottom electrodes under tip contacts in probe station to avoid potential short circuit problems due to tip damage to the device. The molecular DFT calculations were employed to estimate dipole moments, utilizing the Gaussian code alongside the def2-TZVP basis set and the PBE functional. The calculated dipole moment of PT molecule is 8.07 Debye (Figure 2b), which contributes to its excellent ferroelectric properties. Atomic force microscope (AFM) of the PT film (Figure 2c) reveals a surface roughness of ≈0.9 nm, indicating that the spin coated PT film is of high uniformity with low roughness. In Figure 2d, PT film presents a typical P-E hysteresis loop (blue line) with saturated polarization (P_s) of 3.6 μC cm^{-2}. The current-electric field curve plotted next to the P—E hysteresis loop reveals two oppositely polarized peaks that originate from the

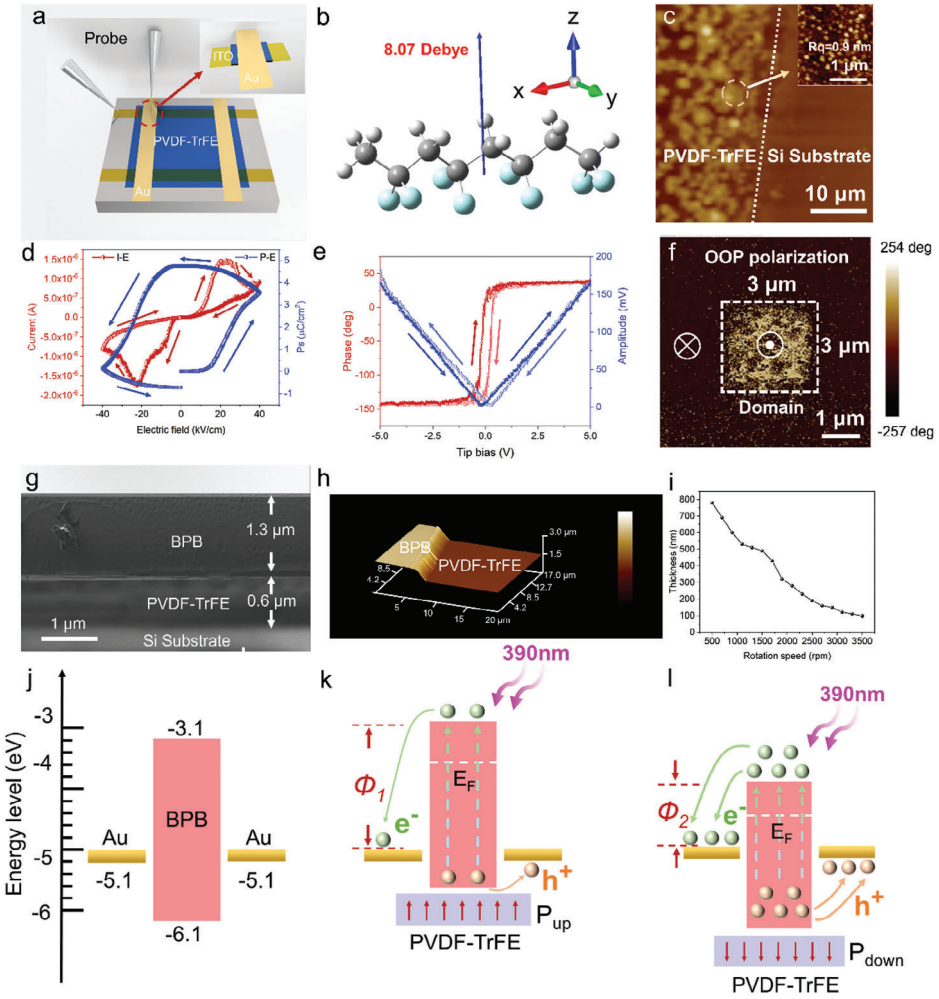

Figure 2. Ferroelectric performance of PT and van der Waals heterostructure characterization of BPB/PT. a) Schematic diagram of testing system of PT film. b) Molecular structure of PT and its calculated dipole moment. c) AFM image of PT film. d) P—E hysteresis loop and I—E curve of PT film. e) The butterfly-shaped piezoelectric force microscope (PFM) amplitude loop and 180°-reversed PFM phase loop of PT films (the red line represents phase change and the bule line represents amplitude change). f) The PFM phase image after scanning the grounded PFM tip on the PT films with a +8 V bias in 3×3 μm^2 region. g) Cross-sectional SEM images of BPB/PT heterojuntion on Si substrate. Scale bar:1 μm. h) 3D AFM image of BPB/PT heterojuntion on Si substrate. i) The variation curve of PT film thickness with rotational speed. j) Energy level diagram of the Au/BPB/Au interface. Energy level diagram of the BPB/PT with polarization of k) upward position and l) downward position.

switching of two ferroelectric states. The estimated coercive field (Ec) for the PT film is determined to ±21 kV cm^{-1}, as revealed in the P—E loop. Along with phase contrast imaging, local PFM switching spectroscopy further confirms the robust ferroelectricity in PT films, as demonstrated by 180° phase hysteresis and its butterfly-shape amplitude loops (Figure 2e). The piezoelectric force microscope (PFM) image shown in Figure S14 (Supporting Information) indicates that the initial domain structure of PT is characterized by a homogeneous single-domain configuration. The polarization state of the 3×3 μm^2 PT region polarized with -8 V sample bias is nearly 180° contrast difference to that of the as-grown region, implying that the latter has a ferroelectric polarization pointing toward the top Au electrode, that is, downward self-polarization(Figure 2f) As observed in the SEM cross-sectional image in Figure 2g and t the thickness of BPB is 1.3 μm and the thickness of PT is 0.6 μm, forming an excellent van der Waals contact. Figure 2h presents the 3D AFM image of the BPB/PT heterojuntion on Si substrate. Considering the importance of the thickness of PT film for subsequent heterojunction formation, we measured the thickness of PT film at different rotational speeds. Figure 2i shows the thickness variation of spin coated PT film at different rotational speeds. In the vertical heterojunction formed between ferroelectric thin films and optoelectronic materials, the polarization direction of ferroelectric materials has a significant impact on the band structure, photocurrent, and dark current of optoelectronic materials. This effect is mainly achieved through the modulation of the band bending degree and carrier behavior of optoelectronic materials by the polarization electric field of ferroelectric thin films. The polarization direction (upward or downward) of ferroelectric thin films can change their surface charge distribution, thereby affecting the band structure at the interface of optoelectronic materials. When ferroelectric thin films undergo upward polarization, the positively polarized surface charge of the ferroelectric thin film at the interface will

cause a positive electrostatic potential, which will increase the energy of the conduction and valence bands of the optoelectronic material, causing the energy band at the interface to bend upward. This may reduce the separation efficiency of photogenerated charge carriers, especially in cases where carrier diffusion is limited, resulting in a decrease in photocurrent. In addition, the upward bending of the interface band may reduce the capture effect of the interface composite center, thereby reducing the dark current. The polarization direction (forward or reverse) of ferroelectric thin films can change their surface charge distribution, thereby affecting the band structure at the interface of optoelectronic materials. When ferroelectric thin films undergo forward polarization, the positively polarized surface charge of the ferroelectric thin film at the interface will cause a positive electrostatic potential, which will increase the energy of the conduction and valence bands of the optoelectronic material, causing the energy band at the interface to bend upward. This may reduce the separation efficiency of photogenerated charge carriers, especially in cases where carrier diffusion is limited, resulting in a decrease in photocurrent. In addition, the upward bending of the interface band may reduce the capture effect of the interface composite center, thereby reducing the dark current. When ferroelectric thin films undergo upward polarization, the negatively polarized surface charge of the ferroelectric thin film at the interface will cause a negative electrostatic potential, which will reduce the energy of the conduction and valence bands of the optoelectronic material, causing the energy band at the interface to bend downward, resulting in favorable conditions for electron injection at the interface. This improves the separation efficiency and charge collection efficiency of photogenerated carriers, resulting in an increase in photocurrent. In addition, the downward bending of the interface band may increase the capture effect of the interface composite center, thereby increasing the dark current. Figure 2j shows the initial band diagrams of BPB and Au electrodes. As illustrated in Figure 2k, when PT is polarized upwards, it induces the BPB band to bend upwards, making carrier separation more difficult and efficiency reduced, thereby reducing the photocurrent. As illustrated in Figure 2l, When PT is polarized downwards, it induces the BPB band to bend downwards, promoting carrier separation and increasing photocurrent.

In order to investigate the optoelectronic properties of BPB/PT, PDs based on BPB/PT are fabricated and characterized. The spectral responsivity (R_λ), *EQE*, and specific detectivity (D^*) are critical parameters for optoelectronic performance evaluation.

The spectral responsivity (R_λ) is introduced to evaluate the spectral response performance of perovskite PDs with $n = 1$ to 5, highlighting the response sensitivity to optical signals within a specific wavelength range. R_λ is defined by the following Equation (3):

$$\mathrm{R}_\lambda = \frac{\mathrm{I_{ph}} - \mathrm{I_{dark}}}{\mathrm{P}_\lambda \mathrm{S}} \tag{3}$$

where $\mathrm{I_{ph}}$ is the photocurrent, I_{dark} is the dark current, P_λ is the light power density, and S is the effective irradiation area. Specifically, for BPB/PT

$$R = \frac{I_{ph} - I_{dark}}{P_\lambda S} = \frac{5.8\times10^{-9} - 6.2\times10^{-13}\ A}{400\ \mu m^2 \times 94.7\ \mu W/cm^2} = 15.3\ A/W \tag{4}$$

Apart from the responsivity mentioned above, two additional key parameters-detectivity (D^*) and external quantum efficiency (EQE) are introduced to further evaluate the performance of the PD. D^* represents the sensitivity of the PD to weak signals within a noise environment. The noise current spectrum can provide more comprehensive and accurate noise characteristics by measuring the noise power density of the PD at different frequencies. The detectivity is usually calculated by the following Equation (5):

$$D^* = \frac{\sqrt{S \times f_{-3dB}}}{NEP} \tag{5}$$

where S is the effective illumination area of the PD, $f_{-3\ dB}$ is the -3 dB bandwidth of the PD and NEP is noise equivalent power. The noise spectrum can accurately reflect the actual noise level of the PD, including all frequency dependent noise (such as 1/f noise). Specifically, for BPB/PT,

$$D^* = \frac{\sqrt{S \times f_{-3dB}}}{NEP} = \frac{\sqrt{400\ \mu m^2 \times 970\ \mathrm{kHz}}}{0.98\times10^{-15}\ W/\sqrt{Hz}} = 1.99\times10^{13}\ Jones \tag{6}$$

EQE is the ratio of photogenerated carriers to the number of incident photons, reflecting the optoelectronic conversion efficiency of the PDs. It can be calculated as

$$\mathrm{EQE} = \frac{\mathrm{hc}}{\mathrm{e}_\lambda}\ \mathrm{R}_\lambda \tag{7}$$

where h, c, and λ refer to the Planck constant, light speed, and wavelength.

As shown in **Figure 3**a, the BPB/PT PD yields a low dark current of 6.2×10^{-13} A at a 3 V bias and a photocurrent of up to 5.8×10^{-9} A under 390 nm illumination. In comparison, BPB alone yields a dark current of 3.0×10^{-13} A at same bias and a photocurrent of 3.6×10^{-11} A under same illumination. The significant photocurrent increases of BPB by more than two orders of magnitude (over 10^2) upon contact with PT through van der Waals interaction can be explained by energy level theory (Figure 2i). In Figure 3b, BPB/PT demonstrates a high responsivity of 15.3 A W^{-1} under 390 nm illumination and a high detectivity of 1.99×10^{13} Jones. Figure 3c shows that the BPB/PT achieves a high EQE of 4.9×10^3% at 3 V bias, surpassing the EQE of BPB (Figure S13, Supporting Information). As illustrated in Figure 3d, the semilogarithmic current–voltage (I–V) curves reveal that BPB/PT exhibits a higher photocurrent of 5.6×10^{-9} A compared BPB 3.5×10^{-11} A, Moreover BPB/PT shows a superior on/off ration of 9.3×10^3, compared to BPB's 1.2×10^2. According to Figure 3e, the responsivity and detectivity of BPB are measured to be 0.25 A W^{-1} and 2.62×10^{11} Jones, respectively. Additionally, as demonstrated in Figure 3f and Table S1 (Supporting Information), the BPB/PT PDs in this work exhibit superior photoresponse performance compared to other low-dimensional materials, including traditional semiconductors and hybrid perovskites. Figure 3g–i present the long term I–t test of BPB/PT PDs. It can be seen from the Figure 3h that the PDs maintain a stable photocurrent over 200 cycles of I–t curve. Furthermore, compared to the photocurrent in the first four cycles (Figure 3g), the photocurrent in the last four cycles (Figure 3i) maintains 97.4% of the initial photocurrent, demonstrating excellent

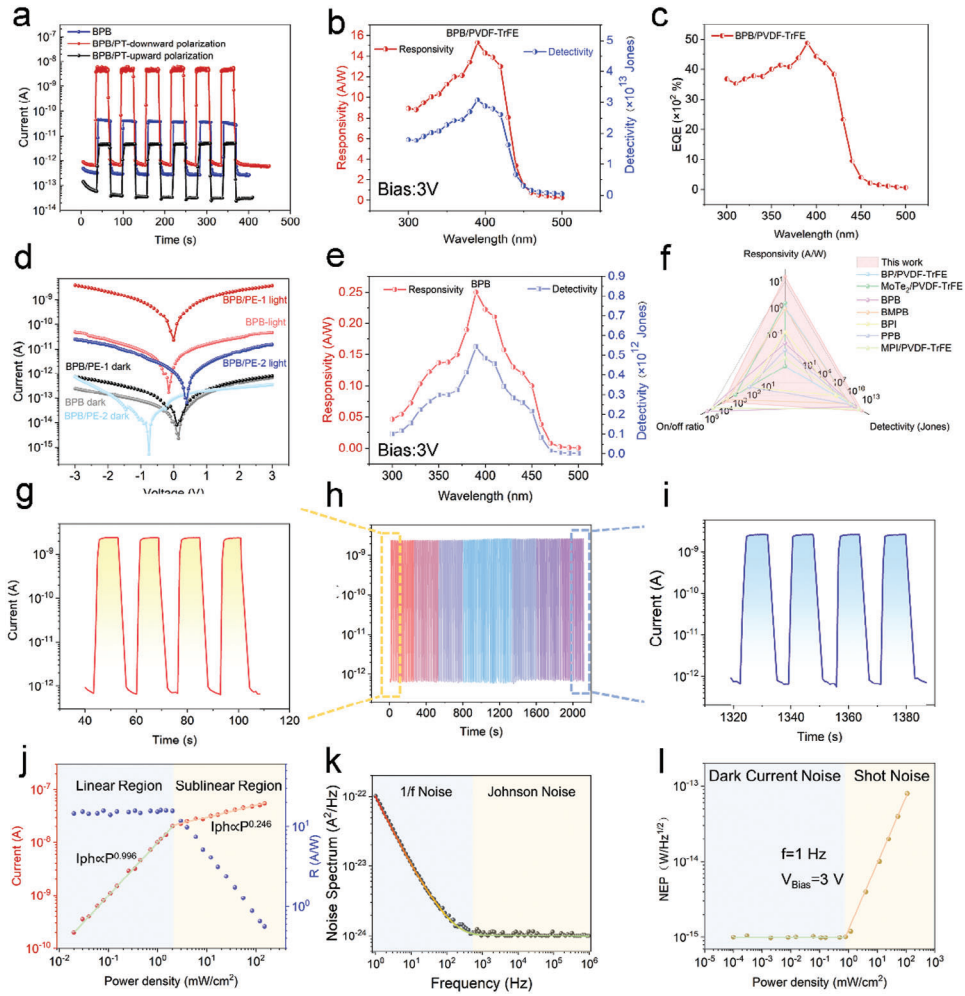

Figure 3. Optoelectronic performance of BPB and BPB/PT. a) *I–t* curves at 3 V bias under 390 nm illumination. b) The responsivity curve and the detectivity curve as a function of wavelength for BPB/PT. Bias: 3V. c) EQE curve at 390 nm illumination of BPB/PT. Bias: 3V. d) *I–V* curves in the dark and under 390 nm illumination. BPB/PT-1 and BPB/PT-2 states represent the downward and upward polarization direction of PT film. e) The responsivity curve and the detectivity curve as a function of wavelength for BPB. f) Responsivity and wavelength of BPB/PT PD and reported PDs in the previous studies. The reference data are from Table S1 (Supporting Information). g) The first four I-t curve cycles of BPB/PT. h) The total 200 continuous response cycles under 390 nm illumination of BPB/PT. i) The last four I-t curve cycles of BPB/PT. j) Photocurrent and responsivity of BPB/PT at different laser power densities of 3 V bias at 390 nm wavelength. k) The noise current spectrum of BPB/PT at 3 V bias. l) NEP of BPB/PT at different laser power densities of 3 V bias under laser irradiation at 390 nm.

stability. In Figure 3j, when the light power density is between 0.018 and 2.03 mW cm^{-2}, the dependence index α of photocurrent on optical power density is ≈0.996, showing a good linear dependence relationship ($\alpha = 1$). When the optical power density exceeds 2.03 mW cm^{-2}, the dependence index α of is 0.246, entering the nonlinear dependence region. Based on this, the LDR can be calculated to be ≈41.4 dB. Figure 3k shows the noise current spectrum of the PD, it can be seen from the figure that the noise current density significantly decreases with increasing frequency when the frequency is between 1 and ≈4×10^2 Hz (low frequency region, colored in light blue). This characteristic is usually dominated by 1/f noise (flicker noise). This noise is related to defects, interface states, or non-uniformity in the detector materials. The presence of low-frequency noise has a significant impact on low-frequency applications such as steady-state measurements or systems with slow signal changes, and optimization measures such as materials improvement or electronic filtering need to be taken. When the frequency is between ≈4×10^2 and ≈10^6 Hz (mid frequency region, colored in light yellow), the curve is flat within this range. In this region, the noise current density is mainly dominated by Johnson noise, including thermal noise and scattering noise. It is independent of frequency and appears as a constant value. Johnson noise usually reflects the basic performance of the device, and reducing this part of the noise can improve the sensitivity of the PD. The NEP curve of BPB/PT is displayed in Figure 3l. The frequency and bias voltage are set to 1 Hz and 3 V, respectively. When light power density is less than ≈1 mW cm^{-2}, the NEP is ≈10^{-15} W/Hz$^{1/2}$. When the light power density is between ≈1 and ≈100 mW cm^{-2}, the NEP increases with the increasing light power density.

Considering the enhancement of BPB's photocurrent after contacting with PT via Van der Waals force, the potential of

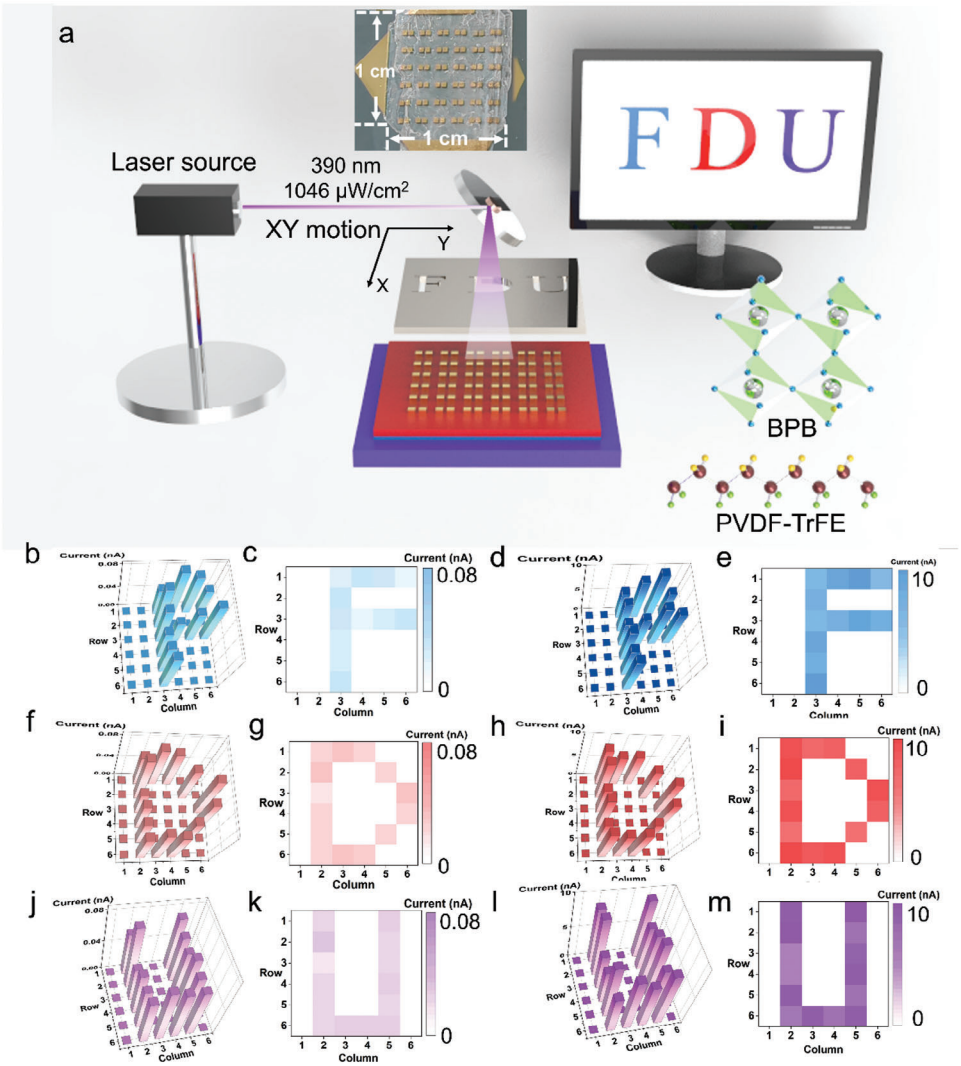

Figure 4. Centimeter-scale PD for different letters imaging process. a) Schematic diagram of large area imaging system of BPB/PT. The inset shows the optical image of BPB/PT centimeter scale imaging device. The 6 × 6 array imaging device of BPB shows the pattern of b) "F", f) "D", j) "U" and corresponding heatmap of c) "F", g) "D", k) "U". The 6 × 6 array imaging device of BPB/PT shows the pattern of d) "F", h) "D", l) "U" and corresponding heatmap of e) "F", i) "D", m) "U".

BPB/PT PDs in large-scale imaging system is explored. As shown in **Figure** 4a, an imaging system has been employed to evaluate the imaging capability of large-scale BPB and BPB/PT PDs. The light source is set to a wavelength of 390 nm and intensity of 1046 μW cm^{-2}. Specifically, images of the letters "F", "D" and "U" patterns are conveyed to the 6 × 6 array PDs via a pixel-by-pixel irradiation imaging method. The inset presents the optical image of BPB/PT PDs. Figure 4b,c displays the photocurrent bar graph and thermal map for the letter "F" in BPB 6 × 6 array PDs, respectively. Figure 4d,e presents the photocurrent bar graph and thermal map for the letter "F" in BPB/PT 6 × 6 array PDs. Likewise, Figure 4f,g depicts the imaging results for the letter "D" in BPB 6 × 6 array PDs, while Figure 4h,i shows the imaging results for the letter "D" in BPB/PT 6 × 6 array PDs. Figure 4j,k illustrates the imaging of the letter "U" in BPB 6 × 6 array PDs, with Figure 4l,m reflect the imaging results for the letter "U" in BPB/PT 6 × 6 array PDs. It can be seen that the photocurrent in BPB/PT PDs surpasses that of BPB PDs, resulting in superior contrast and clarity in the obtained letters image.

Accurately capturing and recognizing object features in light-interference environments poses challenges for conventional image sensors. **Figure** 5a exemplifies a specific scenario: an autonomous vehicle's machine vision system must identify traffic light number on the road, which may be interfered by environmental light. Benefiting from the modulation of ferroelectric polarization, the photocurrent of BPB/PT devices exhibits a switching ratio exceeding three orders of magnitude, along with superior responsivity and stability. When exposed to light interference, the BPB/PT device exhibits more stable image outputs compared to BPB devices (Figure 5b). Specifically, BPB/PT devices maintain stable and recognizable outputs for the numbers "9" and "1" before and after interference, whereas the output of BPB devices becomes difficult to recognize after interference. We input the output images of both into a pre-set neural network

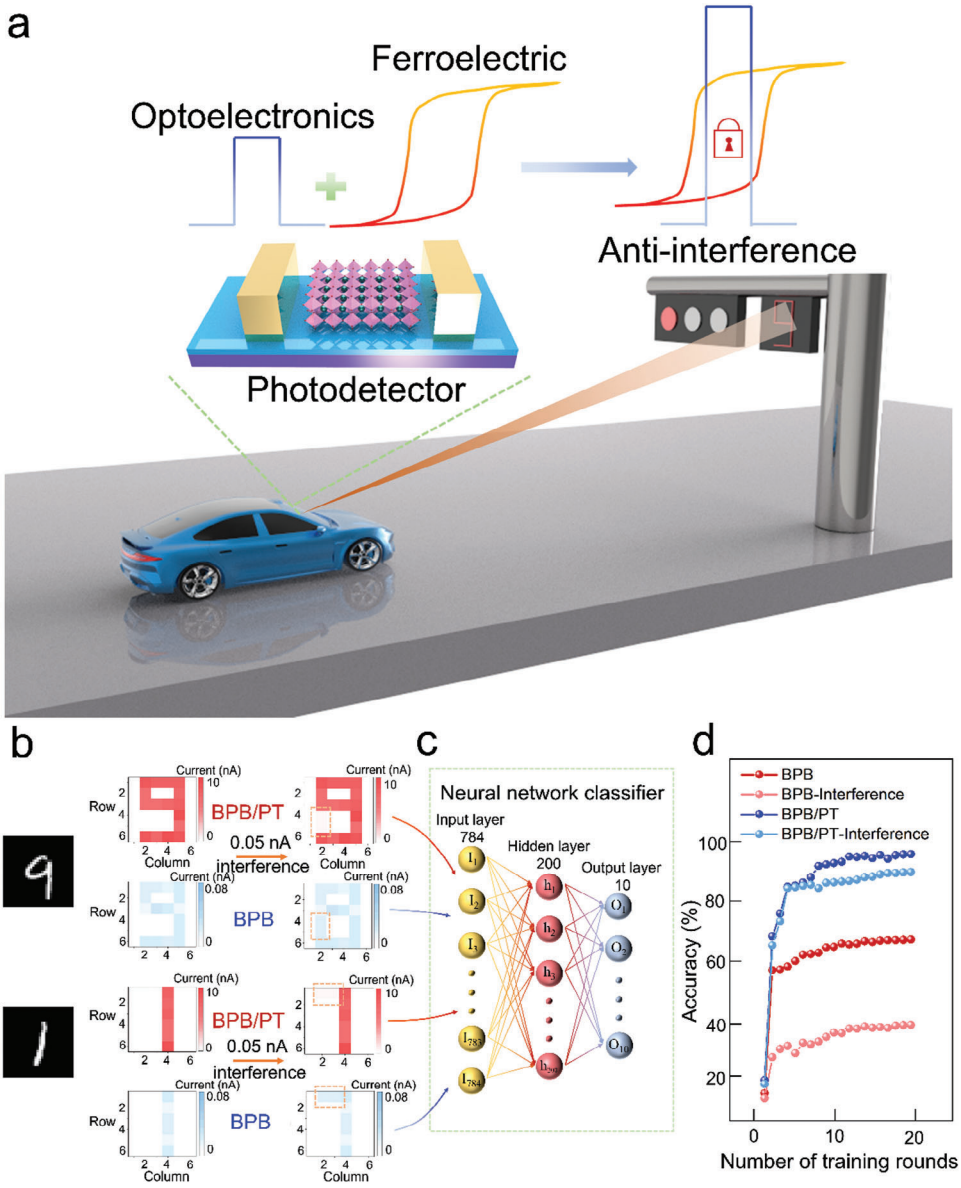

Figure 5. Anti-interference vision system and classifying different numbers. a) Schematic of the application scenario of the BPB/PT anti-interference PD. b) Operational scheme of the anti-interference vision system. The displayed number "9" and "1" images are adapted from MNIST test set. c) A schematic diagram of a three-layer artificial neural network. d) The recognition accuracies of BPB and BPB/PT devices for numbers "9" and "1" before and after interference.

system (Figure 5c). The test results indicate that the accuracy of the output of the BPB/PT device remains above 90% even after 20 rounds of training, while the training accuracy of the output of the BPB device drops to 37% after interference (Figure 5d). These results demonstrate that BPB/PT devices possess robust anti-interference detection capabilities, thereby enhancing the reliability of machine vision in challenging lighting conditions. In addition to its application in anti-interference light imaging system, it also has potential application value in biomedical imaging and light communication. Biomedical applications can be applied to fluorescence imaging and time-resolved fluorescence lifetime imaging to detect the light emitted by biomolecules labeled with fluorescent dyes or quantum dots, and to use fast response PDs to detect fluorescence lifetime for studying molecular environment and metabolic activity. In terms of light communication, it can be used to receive laser signals transmitted in free space, suitable for wireless path communication or encrypted communication. In terms of large-scale applications and environmental stability, the current challenges include: 1) Manufacturing uniformity. 2D perovskites materials are prone to defects during growth and processing, which can affect PD performance. 2) Temperature and humidity sensitivity. Moisture and oxygen in the environment can cause material oxidation or degradation, especially for 2D organic-inorganic hybrid perovskite materials. The potential solutions include: 1) Introducing low-cost manufacturing processes such as inkjet printing, organic

material PD processes, and silicon PD technology. 2) Using wafer level processes (such as silicon-based heterojunction integration) to achieve large-scale production compatible with CMOS processes. 3) Adopt high-quality airtight packaging (such as ceramic or glass packaging) to prevent moisture and oxygen from entering. 4) Integrated thermal management systems, such as thermoelectric cooling (TEC) or heat sinks, maintain stable operating temperatures.

3. Conclusion

In summary, we successfully synthesized 2D BPB perovskites single crystals with a size of 2cm × 1 cm using the quasi-static cooling crystallization method. After forming a heterojunction PD with PT film through van der Waals force, the device exhibited excellent responsivity (15.3 A W^{-1}) and detectivity (1.99×10^{13} Jones) under 390 nm illumination at 3 V bias, and maintained excellent stability over long term I-t cycles (97.4% of the initial photocurrent after 200 cycles). By utilizing this feature, we achieved a multifunctional large-area centimeter level imaging system application. The heterojunction systems exhibit superior imaging quality, which is expected to be applied in autonomous driving anti-interference detection systems. After the input of interference, PDs trained with neural networks can maintain a detection accuracy exceeding 90%. This design method is also applicable to other 2D RP perovskites devices, significantly contributing to advancements in anti-interference photodetection.

4. Experimental Section

Reagents: BABr (99.99%), MABr (99.99%), $PbBr_2$ (≥98.0%), Hydrobromic acid (HBr, 55.0-58.0% in H_2O, contains≤1.5%H_3PO_2), PT (70:30, mol%) were used as reagents without further treatment.

Crystal Growth and Device Construction—Crystal Growth: Single-crystalline BPB was synthesized from concentrated HBr solutions containing stoichiometric quantities of BABr (1.176 g), $PbBr_2$ (2.808 g). The clear solutions were obtained after reaction for 0.5 h at 110 °C. Large-size single crystals were grown by the temperature lowering method from saturated solution. The cooling rate was 2 °C day^{-1}. The high-quality crystals could be obtained after 30 days.

Device Construction: PT ferroelectric thin film was prepared on Si substrate using spin coating method, with a spin coating rate of 3000 rpm. PT is dissolved in DMF solvent with a mass fraction of 1%. After drying the solvent at 80 °C, transfer the grown BPB single crystal onto the PT film, fix the crystal with polyimide tape, and then polarize the ferroelectric thin film using electrospinning equipment (E = 40 kV cm^{-1}). Subsequently, a 6 × 6 array gold electrode was deposited by thermal evaporation.

Materials Characterization and Ferroelectric-Optoelectronic Measurement: The optical images were captured by Olympus microscope. PL spectra were acquired by Renishaw inVia-Qontor Raman microscope equipped with 325 and 532 nm lasers. Transmission electron microscope (TEM, JEM-F200), high-resolution TEM (HRTEM) and selected area electron diffraction (SAED) were used to characterize the crystal structure. The composition determination of crystal materials was carried out by a Bruker D8 Advance X-ray Power diffractometer (XRD, Cu-Kα radiation source, λ = 1.5406 nm). The optical properties were obtained using an UV-vis spectrometer (Hitachi U-3900H) and a FLS1000 fluorescence spectrometer. XPS spectra were obtained using Thermo ESCALAB 250XI under the excitation of Al Kα (energy = 1486.6 eV, voltage = 15 kV, beam current = 10 mA). The height and roughness data were measured by step profiler (Bruker DektakXT) and atomic-force microscope (AFM). The morphologies of perovskites microplates were obtained by using a ZEISS laser scanning confocal microscope (LSM 900). A dual channel precision sourcemeter (2902A, Keysight) was used for the electrical measurement in air. The domain patterns obtained after poling using positive/negative voltages were inspected via out-plane piezoresponse force microscopy (PFM) amplitude and phase imaging (Icon, Bruker) using a contact PtIr-coated silicon tip with a radius of ≈20 nm, a force constant of 2.8 N m^{-1}, and an AC amplitude of 1 V at 386 kHz. The optoelectronic properties were collected using the semiconductor characterization system (Keithley 4200-SCS) connected a vacuum probe station (Lake Shore) and a 75 W Xe lamp equipped with a monochromator was used as light source. The light density was measured by a NOVA II power meter (OPHIR photonics). The wavelength and light intensity used in the PDs comparison are 390 nm and 1647 μW cm^{-2}. All the measurements were tested at room temperature.

Supporting Information

Supporting Information is available from the Wiley Online Library or from the author.

Acknowledgements

The work was supported by the National Key R&D Program of China (No. 2022YFA1402904), the National Natural Science Foundation of China (No. 62374035, 92263106 and 52425308).

Conflict of Interest

The authors declare no conflict of interest.

Data Availability Statement

The data that support the findings of this study are available in the supplementary material of this article.

Keywords

2D Ruddlesden-Popper perovskites, ferroelectric, photodetector, PVDF-TrFE, single-crystal

Received: December 16, 2024
Revised: December 26, 2024
Published online:

[1] Y. C. Kim, K. H. Kim, D. Y. Son, D. N. Jeong, J. Y. Seo, Y. S. Choi, I. T. Han, S. Y. Lee, N. G. Park, *Nature* **2017**, *550*, 87.
[2] D. Pan, Y. Fu, N. Spitha, Y. Zhao, C. R. Roy, D. J. Morrow, D. D. Kohler, J. C. Wright, S. Jin, *Nat. Nanotechnol.* **2021**, *16*, 159.
[3] Y. Hu, Z. Q. Li, X. S. Fang, *J. Inorg. Mater.* **2023**, *38*, 1055.
[4] J. Hu, L. Yan, W. You, *Adv. Mater.* **2018**, *30*, 1802041.
[5] E. Hong, Z. Li, X. Zhang, X. Fan, X. S. Fang, *Adv. Mater.* **2024**, *36*, 2400365.
[6] Z. Ou, C. Wang, Z. G. Tao, Y. Li, Z. Li, Y. Zeng, Y. Li, E. Shi, W. Chu, T. Wang, H. Xu, *Nano Lett.* **2024**, *24*, 5975.
[7] Y. Liang, F. Liu, X. Xie, Y. Ma, Y. Guan, W. Yu, Y. Zou, L. Zhang, X. Zhang, Y. Zhang, B. Li, C. Wu, K. Jiang, L. Xiao, D. Zou, S. Zheng, *Adv. Funct. Mater.* **2024**, *34*, 2401257.
[8] H. Chen, Z. Zhu, B. Zhao, W. Huang, G. Qu, Z. X. Xu, X. F. Yu, Q. Xiao, S. Yang, Y. Li, *Adv. Sci.* **2024**, *11*, 2309185.

[9] S. Wang, Y. Chen, J. J. Yao, G. X. Zhao, L. Z. Li, G. F. Zou, *J. Mater. Chem. C* **2021**, *9*, 6498.
[10] S. Guo, W. Mihalyi-Koch, Y. Mao, X. Li, K. Bu, H. Hong, M. P. Hautzinger, H. Luo, D. Wang, J. Gu, Y. Zhang, D. Zhang, Q. Hu, Y. Ding, W. Yang, Y. Fu, S. Jin, X. Lu, *Nat. Commun.* **2024**, *15*, 3001.
[11] R. Mastria, K. J. Riisnaes, A. Bacon, I. Leontis, H. T. Lam, M. A. S. Alshehri, D. Colridge, T. H. E. Chan, A. De Sanctis, L. De Marco, L. Polimeno, A. Coriolano, A. Moliterni, V. Olieric, C. Giannini, S. Hepplestone, M. F. Craciun, S. Russo, *Adv. Funct. Mater.* **2024**, *34*, 2401903.
[12] J. Zhang, J. Li, J. Duan, X. Zhang, J. Dou, Q. Guo, C. Jiang, Y. Zhao, H. Huang, Q. Tang, *Adv. Funct. Mater.* **2024**, *34*, 2401662.
[13] W. Li, M. Li, Y. He, J. Song, K. Guo, W. Pan, H. Wei, *Adv. Mater.* **2024**, *36*, 2309588.
[14] C. Wan, Z. Wang, H. Zhang, S. Tie, Z. Liang, H. Xu, Y. Ma, Z. Wang, X. Zheng, X. Pan, J. Ye, *Adv. Funct. Mater.* **2024**, *34*, 2401220.
[15] L. Min, H. Sun, L. Guo, Y. Zhou, M. Wang, F. Cao, L. Li, *Adv. Mater.* **2024**, *36*, 2400279.
[16] J. Zhong, D. Zhou, Q. Bai, C. Liu, X. Fan, H. Zhang, C. Li, R. Jiang, P. Zhao, J. Yuan, X. Li, G. Zhan, H. Yang, J. Liu, X. Song, J. Zhang, X. Huang, C. Zhu, C. Zhu, L. Wang, *Nat. Commun.* **2024**, *15*, 3185.
[17] S. Chowdhury, M. K. Mukhopadhyay, M. K. Sanyal, S. Bhunia, B. Satpati, R. P. Giri, B. Bharatiya, C. Shen, B. M. Murphy, *Adv. Funct. Mater.* **2024**, *34*, 2401334.
[18] K. Yang, Y. Kang, S. Meng, J. Zhang, W. Ma, *Nano Lett.* **2024**, *24*, 5057.
[19] K. Dong, X. Yang, F. Yao, H. Cong, H. Zhou, S. Zhou, H. Cui, S. Wang, C. Tao, C. Sun, H. Fu, W. Ke, G. Fang, *Adv. Mater.* **2024**, *36*, 2313889.
[20] M. Esmann, S. C. Wein, C. Antón-Solanas, *Adv. Funct. Mater.* **2024**, *34*, 2315936.
[21] L. Li, Z. Sun, P. Wang, W. Hu, S. Wang, C. Ji, M. Hong, J. Luo, *Angew. Chem. Int. Ed.* **2017**, *56*, 12150.
[22] S. Han, J. Bie, W. Fa, S. Chen, L. Tang, W. Guo, H. Xu, Y. Ma, Y. Liu, X. Liu, Z. Sun, J. Luo, *J. Am. Chem. Soc.* **2024**, *146*, 8298.
[23] J. Y. Zheng, X. Y. Song, Y. R. Wu, Y. L. Lian, Y. Q. Li, Q. T. Xu, Y. Zhou, Z. Y. Wang, L. Wang, J. H. Luo, S. E. Zhao, *Adv. Funct. Mater.* **2024**, *34*, 2403843.
[24] Q. Fan, Y. Ma, S. You, H. Xu, W. Guo, Y. Liu, L. Tang, W. Li, J. Luo, Z. Sun, *Adv. Funct. Mater.* **2023**, *34*, 2312395.
[25] R. Li, Z. Wang, T. Zhu, H. Ye, J. Wu, X. Liu, J. Luo, *Angew. Chem. Int. Ed.* **2023**, *62*, 202308445.
[26] L. Tang, W. Weng, H. Chen, L. Hua, W. Guo, Y. Liu, Y. Ma, Y. Chen, J. Luo, Z. Sun, *Adv. Funct. Mater.* **2023**, *33*, 2214858.
[27] X. He, S. Hao, D. Ouyang, S. Liu, N. Zhang, Z. Zeng, Y. Zhang, I. Spanopoulos, C. Wolverton, Y. Li, T. Zhai, *Adv. Funct. Mater.* **2024**, *34*, 2313163.
[28] Y. Wang, T. Guo, J. Yin, Z. Tian, Y. Ma, Z. Liu, Y. Zhu, H. N. Alshareef, *Adv. Mater.* **2022**, *34*, 2106937.
[29] Y. Zhang, X. Y. Zhao, J. X. Chen, S. Y. Li, W. Yang, X. S. Fang, *Adv. Funct. Mater.* **2020**, *30*, 1907650.
[30] J. Zha, S. Shi, A. Chaturvedi, H. Huang, P. Yang, Y. Yao, S. Li, Y. Xia, Z. Zhang, W. Wang, H. Wang, S. Wang, Z. Yuan, Z. Yang, Q. He, H. Tai, E. H. T. Teo, H. Yu, J. C. Ho, Z. Wang, H. Zhang, C. Tan, *Adv. Mater.* **2023**, *35*, 2211598.
[31] J. Wang, C. Liu, L. Zhang, J. Chen, J. Chen, F. Yu, Z. Zhao, W. Tang, X. Li, S. Zhang, G. Li, L. Wang, Y. Cheng, X. Chen, *Adv. Sci.* **2023**, *10*, 2205813.
[32] K. H. Kim, S. Oh, M. M. A. Fiagbenu, J. Zheng, P. Musavigharavi, P. Kumar, N. Trainor, A. Aljarb, Y. Wan, H. M. Kim, K. Katti, S. Song, G. Kim, Z. Tang, J. H. Fu, M. Hakami, V. Tung, J. M. Redwing, E. A. Stach, R. H. Olsson, D. Jariwala, *Nat. Nanotechnol.* **2023**, *18*, 1044.
[33] H. Wang, Y. Song, G. Huang, F. Ding, L. Ma, N. Tian, L. Qiu, X. Li, R. Zhu, S. Huang, H. Yan, X. H. Chen, L. Ding, C. Zheng, W. Ruan, Y. Zhang, *Nat. Mater.* **2024**, *23*, 470.
[34] Z. Chen, W. Li, Z. Fan, S. Dong, Y. Chen, M. Qin, M. Zeng, X. Lu, G. Zhou, X. Gao, J. M. Liu, *Nat. Commun.* **2023**, *14*, 3585.
[35] T. Sun, R. Chen, W. Ma, H. Wang, Q. Yan, J. Luo, S. Zhao, X. Zhang, P. Li, *Nat. Nanotechnol.* **2024**, *19*, 758.
[36] Z. Liu, H. Wang, M. Li, L. Tao, T. R. Paudel, H. Yu, Y. Wang, S. Hong, M. Zhang, Z. Ren, Y. Xie, E. Y. Tsymbal, J. Chen, Z. Zhang, H. Tian, *Nature* **2023**, *613*, 656.
[37] L. Su, T. T. Yan, X. Y. Liu, F. Cao, X. S. Fang, *Adv. Funct. Mater.* **2023**, *33*, 2214533.
[38] F. Cao, W. Tian, M. Wang, H. Cao, L. Li, *Adv. Funct. Mater.* **2019**, *29*, 1901280.
[39] S. Kim, S. Lee, S. Oh, K. B. Lee, J. J. Lee, B. Kim, K. Heo, J. H. Park, *Small* **2024**, *20*, 2305045.
[40] P. Sharma, D. Wu, S. Poddar, T. J. Reece, S. Ducharme, A. Gruverman, *J. Appl. Phys.* **2011**, *110*, 052010.
[41] J. Liu, L. Su, X. Zhang, D. V. Shtansky, X. S. Fang, *Small Methods* **2024**, *8*, 2300319.
[42] D. Li, J. K. Qin, B. Zhu, L. Q. Yue, P. Y. Huang, C. Zhu, F. Zhou, L. Zhen, C. Y. Xu, *ACS Nano* **2024**, *18*, 9636.
[43] C. M. Song, D. Kim, S. Lee, H. J. Kwon, *Adv. Sci.* **2024**, *11*, 2308588.
[44] G. Sanchez-Santolino, V. Rouco, S. Puebla, H. Aramberri, V. Zamora, M. Cabero, F. A. Cuellar, C. Munuera, F. Mompean, M. Garcia-Hernandez, A. Castellanos-Gomez, J. Iniguez, C. Leon, J. Santamaria, *Nature* **2024**, *626*, 529.
[45] X. Wang, P. Wang, J. Wang, W. Hu, X. Zhou, N. Guo, H. Huang, S. Sun, H. Shen, T. Lin, M. Tang, L. Liao, A. Jiang, J. Sun, X. Meng, X. Chen, W. Lu, J. Chu, *Adv. Mater.* **2015**, *27*, 6575.